Catalysis Today 369 (2021) 48–61

Contents lists available at ScienceDirect

Catalysis Today

journal homepage: www.elsevier.com/locate/cattod

Effects of metal dusting relevant exposures of alloy 601 surfaces on carbon formation and oxide development

Xiaoyang Guo [a], Estelle Vanhaecke [a], Per Erik Vullum [b], Jianyu Ma [a], P. V. Daham S. Gunawardana [a,1], John C. Walmsley [b,2], De Chen [a], Hilde J. Venvik [a,*]

[a] Department of Chemical Engineering, NTNU - Norwegian University of Science and Technology, Trondheim, 7491, Norway
[b] SINTEF Industry, Trondheim, 7465, Norway

ARTICLE INFO

Keywords:
carbon formation
metal dusting
synthesis gas alloy 601
chromium oxide
spinel

ABSTRACT

Ni and Fe are excellent catalysts for carbon formation, and industrial alloys are therefore susceptible to metal dusting corrosion; a costly issue in e.g. synthesis gas manufacture. The objective of this work is to better understand the initial reaction phenomena leading to metal dusting, and thereby minimize the corrosion through optimum alloy selection and pretreatment. Pre-oxidized alloy 601 samples were subjected to carburizing gaseous environments at 750 °C, and carbon formation and surface oxide layer development were investigated by SEM, optical microscopy, AES and Raman spectroscopy. Thin (S)TEM/EDS cross-section lamellae were prepared by Focussed Ion Beam milling.

Beyond the initial incubation period, less carbon is formed under 10% CO/Ar than under synthesis gas with finite low carbon activity. Cr_2O_3 evolves as a thin surface oxide layer with only CO reacting and more ordered carbon develops with increasing exposure time. In contrast, oxidation yields (Ni, Fe, Cr)$_3O_4$ spinel formation while the materializing carbon remains its disorder during prolonged exposure to synthesis gas. The metal dusting corrosion rate is hence lowered due to Cr_2O_3 stabilization, while the spinel represents an unstable redox state that continuously yields new carbon. A fine-grained alloy surface structure is also found beneficial to the Cr_2O_3 formation.

1. Introduction

Fe, Ni and Co are known as catalysts for producing carbon nanotubes and carbon nanofibers due to their ability to activate gaseous carbon-containing molecules to form carbon-carbon bonds. In the petrochemical industries, metals and alloys are typically exposed to carbon-saturated gaseous environments with low partial pressures of oxygen and/or steam in a critical temperature range of 400–900 °C [1–4]. Fe and Ni are also main constituent elements of common industrial alloys with desirable high temperature stability. Equipment based on these alloys is therefore susceptible to so-called metal dusting corrosion; a detrimental degradation phenomenon that proceeds by a gradual breakdown of the material into a powdery mixture of graphite, carbide and metal particles. Metal dusting carries significant cost, since considerable measures need to be implemented in order to avoid catastrophic events in the industrial operation.

One of the measures that are being applied to prevent metal dusting (as well as other) corrosion is the incorporation of chromium (Cr) in the alloy to facilitate the formation of a Cr oxide at the surface. Cr_2O_3 is known as impermeable to carbon and remains stable in carbonaceous and reducing atmospheres down to very low oxygen partial pressure [5]. Surface layers of Cr_2O_3 are excellent in preventing alloys from metal dusting corrosion [6,7] provided a dense and defect free oxide layer that prohibits access to the bulk matrix can be formed and maintained during industrial operation. Manganese (Mn) is another alloying element in high temperature alloys, known to suppress the hot working brittleness. High mobility of Mn in Cr_2O_3 [8] enables formation of a $CrMn_2O_4$ spinel phase, and this spinel is also established as a good protective scale [9–13].

The phenomenon of metal dusting has been studied for decades [4, 14–20]. Metal dusting of Fe-based alloys has been shown to involve metastable Fe_3C formation and the subsequent decomposition [18,21]

* Corresponding author.
E-mail address: hilde.j.venvik@ntnu.no (H.J. Venvik).
[1] Present address: Yara International ASA, Hydrovegen 67, 3936 Porsgrunn, Norway.
[2] Present address: Department of Materials Science and Metallurgy, University of Cambridge, 27 Charles Babbage Road, Cambridge CB3 0FS, United Kingdom.

https://doi.org/10.1016/j.cattod.2020.04.029
Received 15 October 2019; Received in revised form 30 March 2020; Accepted 6 April 2020
Available online 16 April 2020

and/or disintegration [7,22] of this compound. The resulting nanoparticles serve as catalysts for further carbon deposition. It should be noted that Ni-based alloys show better metal dusting corrosion resistance compared to Fe-based alloys. There are several reasons for this difference. Cr atoms diffuse relatively fast within the alloy and the amount of Cr increases with the Ni content [23]. Unlike Fe-based alloys, Ni-based alloys do not form metastable M_3C (M = metal) intermediates during the carburization [24]. The carbon permeability is lower in Ni-based alloys compared to Fe-based alloys [16,18,25,26]. Finally, fewer and larger metal particles are formed during the metal dusting process on Ni-based alloys compared to on Fe-based alloys, thereby lowering the total catalytic surface area for carbon formation [16,27]. Once graphite has formed, Ni atoms may diffuse via intercalation to form nanoparticles that catalyze further carbon deposition [17].

Ni-based Inconel 601 generally displays resistance against corrosion under oxidizing and reducing conditions at high temperature [20, 28–39]. Inconel 601 is thus widely used in petrochemical and other process equipment, and several investigations have addressed its susceptibility to metal dusting. Klarstrom et al. have exposed Inconel 601 to a flowing gas mixture for 10,000 hours to find significant metal wastage in the form of numerous rounded pits with diameter up to 1.2 mm. [28]. Walmsley et al. have studied the basic features of carburization and carbide oxidation of Inconel 601 alloy exposed to metal dusting conditions for 2 years in a commercial methanol plant [37]. Nishiyama et al. compared alloy 601 to their own NSSMC 696 alloy under synthesis gas for more than 10,000 hours and concluded that the pits observed occur earlier and grow faster on 601 [29]. Many of these studies have been based on the analysis of long-term exposed material (both in laboratory and in industrial plant), however, the mechanism of the initial carbon formation on the metal dusting relevant alloy surface is less described, documented and understood.

The overall objective of our research is to provide a better general understanding and prediction of carbon formation phenomena leading to metal dusting, as well as enabling alloy selection and alloy pretreatment protocols that minimize metal dusting corrosion. We have previously demonstrated in a qualitative way that the tendency to form solid carbon on the Inconel 601 surface is strongly linked to the pre-oxidation conditions, through the composition and structure of the Cr-rich oxide layer formed [20,38,39]. The carbon formation was catalyzed by Fe and/or Ni (alloy) particles, seemingly originating from the reducible phases presence within this layer [20]. Moreover, we exposed the Inconel 601 to a model syngas at varying temperature to show that pitting features, observed in alloys applied in industrial process equipment, could be formed within relatively short exposures [20]. In this study, by varying the exposure time, we assess the point at which the reducible phases are initiating the first carbon formation as well as how the carbon formation progresses during the initial phase. CO is the main source of carbon, but the effects of adding common synthesis gas components (H_2, CO_2 and H_2O) are also addressed. Characterization by SEM, XRD, Raman and TEM, the latter involving advanced sample preparation by Focused Ion Beam (FIB) milling and EDS/EELS elemental analysis, are combined to yield information on the amount and type of carbon evolving, the nature of the catalyst particles associated with the formation of carbon, the composition and topology of the oxide phases developing at and near the surface during exposure, and finally the characteristics of the initial pitting.

2. Materials and methods

Inconel 601 alloy samples with dimension $15 \times 8 \times 0.5$ mm^3 were cut and first subjected to a procedure intended to yield a consistent and bulk representative starting point. Gradually finer polishing was applied until reaching 1 μm diamond grain size, then ultrasonic cleaning in 99% hexane for 30 min and drying overnight. Oxidation and carburization exposures were thereafter conducted in an experimental setup described elsewhere with a vertical, internally gold-coated, steel tube (Incoloy 800 H) enclosed in a furnace [40].

Oxidation of the alloy samples was performed by ramping the temperature by 10 °C/min in 10% steam in Ar to 540 °C, and then the samples were kept at 540 °C for 6 h at 1 bar. The resulting samples were either unloaded for characterization or exposed to carburizing conditions at 750 °C. Two different gas mixtures (100 Nml/min total flow rate) were used for the experiments; one representing infinite carbon activity ($a_c \gg 1$) and consisting of 10% CO in Ar at 1 bar (denoted as I-a_c), the other simulating syngas at industrially relevant conditions, i.e. finite low carbon activity ($a_c \sim 7$, denoted as FL-a_c), and containing a mixture of H_2 (25%), CO (20%), CO_2 (15%), H_2O (10%) and Ar (30%) at 20 bar total pressure [40]. The metal dusting exposure time varied from 1 h to 20 h. After oxidation/exposure, the samples were cooled under Ar flow and unloaded at ambient conditions.

The resulting samples were characterized by a range of techniques to relate the carbon formation propensity and potential progression of the metal dusting to the initial structure and composition, as well as the development of the metal/oxide matrix during the carburizing exposures. A Zeiss Ultra 55 LE thermal field emission gun scanning electron microscope (FEG-SEM) was operated at 10 kV. The depth profiles of Inconel 601 before and after oxidization were analyzed by Auger spectroscopy under Ar-ion sputtering in a field emission JEOL 9500 F instrument. The acceleration voltage of the electron beam was 10 keV and analysis was performed at 30° under Ar^+ of 1 keV. Raman spectra were collected by focusing a Horiba Jobin Yvon LabRAM HR800 spectrometer, using the emission line at 633 nm from a He-Ne laser, on the sample with a 50 × LWD objective with a motorized x-y stage. The output power of the laser was 8 mW with a spot diameter of approximately 1.5 μm. The spectra were recorded with continuous scans in the range 300-3000 cm^{-1}. Spectra were taken at three different locations on a given sample to verify that the observed surface characteristics were uniform and representative. Grazing incidence X-ray diffraction (XRD) was applied to investigate the near surface region of the samples using a Bruker D8 A25 DaVinci X-ray Diffractometer with Cu Kα radiation with a 1° incidence angle.

Finally, cross-section TEM lamellae were prepared from selected samples by a FEI Helios G4 UX focused ion beam (FIB). Carbon or platinum protection layers (the first part of the layer made by e-beam assisted deposition to avoid ion-beam induced surface damage) were deposited on the selected regions prior to cutting out the TEM lamella. Coarse thinning was performed at 30 kV acceleration voltage. The last part of the thinning was performed at 5 kV and finally 2 kV to minimize ion-beam induced surface damage on either side of the TEM lamellae. The TEM analysis was done on a double C_s aberration corrected cold FEG JEOL ARM 200 F, operated at 200 kV and equipped with a large solid angle Centurio SDD (0.98 sr) for X-ray energy dispersive spectroscopy (EDS) and a Quantum ER GIF for dual electron energy loss spectroscopy (EELS).

3. Results and Discussion

3.1. Initial structure and composition

The nature of the surface oxide layer, i.e. microstructure and composition as resulting from the initial polishing to uncover the bulk and subsequent oxidation in steam at elevated temperature, represents the starting point of this investigation. Fig. 1(a) shows a SEM micrograph of the oxide layer for the pre-oxidized alloy sample before exposure to the carburizing mixture. The parallel streaky features appearing on the alloy surface result from the polishing. Particle-like features can also be observed, and these were formed upon the steam exposure. The corresponding X-ray diffractogram (Fig. 1(b)), displays two strong diffraction peaks from the fcc bulk alloy matrix. Peaks representative of oxides are practically undetectable. The particles are seemingly also recognizable in the Raman optical microscope as the darker features of the image shown in Fig. 1(c). Raman spectroscopy was performed at the

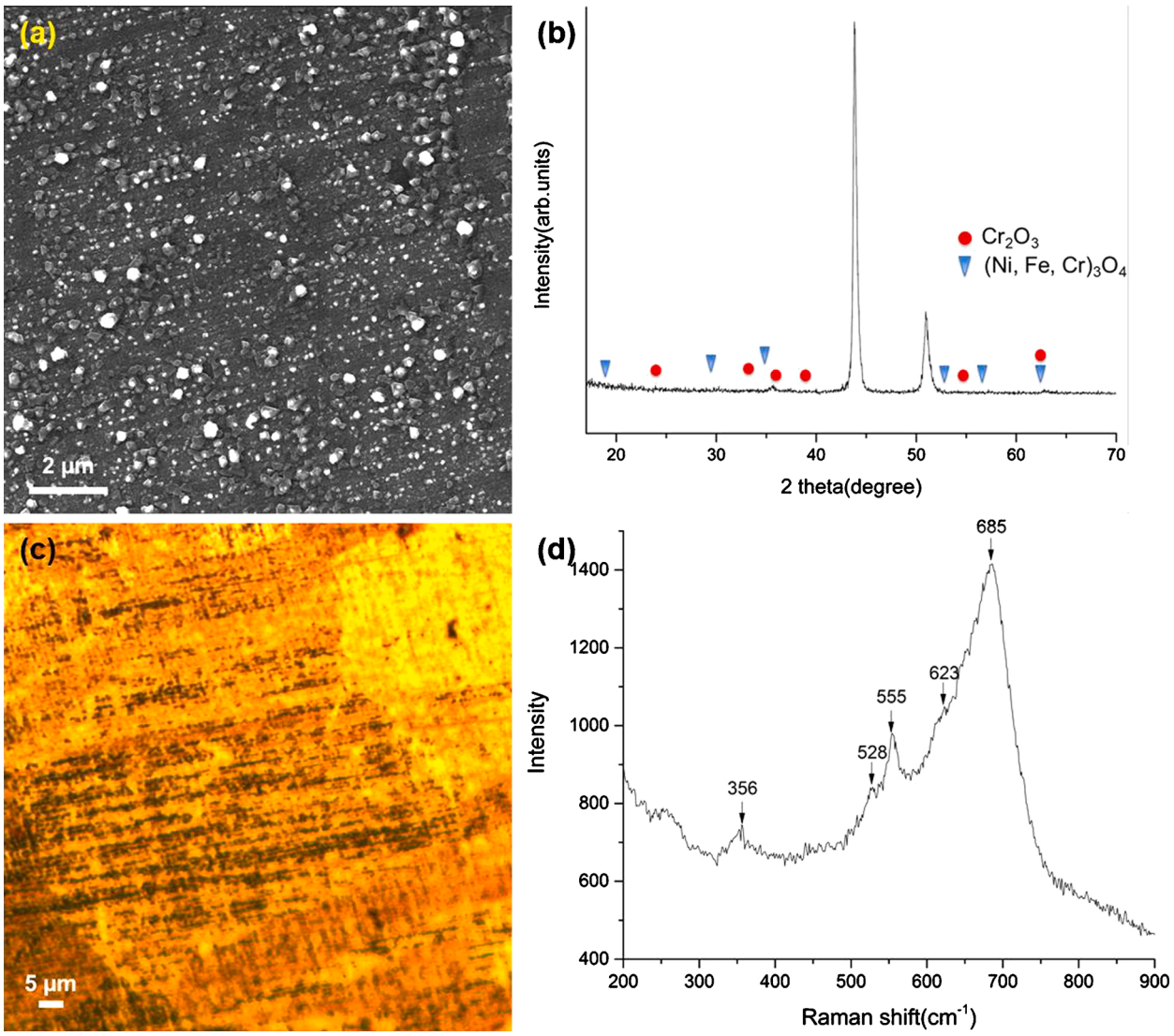

Fig. 1. Surface characterization of polished Inconel 601 sample after oxidation under 10% steam in Ar at 540 °C for 6 h at 1 bar; (a) SEM micrograph; (b) X-ray diffraction (c) Raman optical micrograph; (d) Raman spectroscopy.

center of Fig. 1(c), with the result given in Fig. 1(d). The Raman bands at 358 cm^{-1}, 528 cm^{-1}, 555 cm^{-1}, 623 cm^{-1} correspond to Cr_2O_3 [41], while the peak at 685 cm^{-1} may be assigned to $(Ni, Fe, Cr)_3O_4$ spinel [35]. Spectra from other areas on the sample display similar characteristics.

Auger depth profiles of Inconel 601 before and after oxidization are shown in Fig. 2. It can be noted that the alloy samples also exhibit a very thin oxide layer before oxidization, with thickness ~2 nm, as a result of exposure to ambient conditions during sample transfer. The steam oxidation at 540 °C results in an oxygen rich region of 40-50 nm thickness. The sputtering rate may depend somewhat on the composition and structure of the material [39]. The obtained depth profiles thus provide semi-quantitative information, since the estimated depth refers to sputtering of a SiO_2 standard. The oxide layer estimate corresponds well, however, to thicknesses obtained from TEM cross section analysis of a similar sample (Shown in Fig. S1, Supporting Information), ranging locally from 30 nm to 90 nm. The O concentration decreases when moving from the surface to the bulk alloy matrix. Fig. 2(b) further indicates that the oxidized surface layer is depleted in, but not free from, Fe and Ni, in accordance with the Raman spectroscopy results (Fig. 1 (d)). The amount of Cr relative to Ni and Fe is hence significantly higher than in the bulk.

Combined, the information from Raman spectroscopy and Auger depth profiling shows that a ~40 nm oxide scale has formed after oxidization in 10% steam in Ar. This scale is too thin to yield a significant X-ray diffraction signal, and contains Cr_2O_3 as well as $(Ni, Fe, Cr)_3O_4$ spinel.

3.2. *Carbon formation*

The pre-oxidized alloy samples were subjected to the carburizing gas mixtures at 750 °C as previously described. Carbon formed on the pre-oxidized alloy samples under 1 h to 20 h of infinite carbon activity (1 bar 10% CO in Ar; I-a_c) conditions is illustrated by the SEM micrographs in Fig. 3. Carbon filaments are found after all exposure times. With time, the number of filaments increases as well as the length and the diameter of each filament. The samples exposed for 1 h (Fig. 3(a and b)) display short carbon fibers with nanosized particles at the tip, which is typical of a Ni/Fe catalyzed carbon growth mode. When the exposure time is prolonged to 2 h (Fig. 3(c and d)) a wider range in filament length and diameter is observed. After 5 h exposure time (Fig. 3(e and f)), catalyst particles can be observed not only at the tip of the filaments, but also along the center axis. The twisted morphology of the carbon filaments may have originated from splitting of the catalyst particles. This shape of carbon filaments is more evident after 20 h exposure to the I-a_c

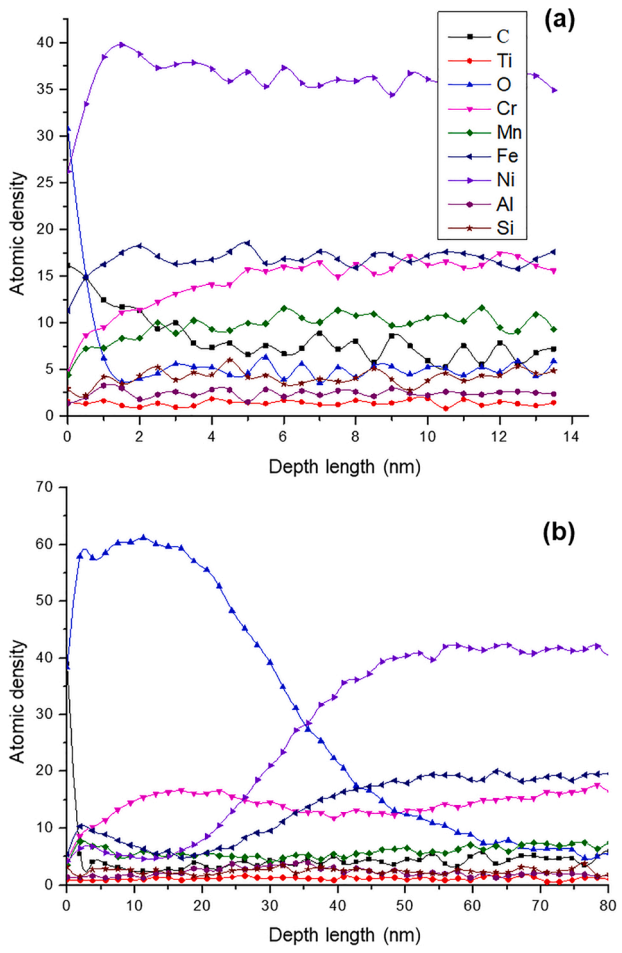

Fig. 2. Auger sputtering depth profiles of polished Inconel 601 surface (a) before oxidization and (b) after oxidization under 10% steam in Ar at 540 °C for 6 h at 1 bar.

conditions (Fig. 3(g and h)). The diameter of the carbon filaments at one end is larger while, as the growth proceeds, the filament diameter gradually decreases. Two different types of catalyst particles were observed associated with these carbon filaments. One is a thin conical shaped nanorod encapsulated at the tip of carbon filaments. The other type includes relatively large, elongated particles encapsulated along the middle of the carbon filaments.

The carbon formation trends after exposures to finite, low carbon activity simulated syngas (20 bar 25% H_2, 20% CO, 15% CO_2, 10% H_2O and 30%Ar; FL-a_c) for 1-20 h are illustrated in Fig. 4. There are no observable carbon filaments after 1 h exposure (Fig. 4(a and b)). After 2 h, short (~100 nm) carbon filaments with catalyst particles at the tip are found (Fig. 4(c and d)). In Fig. 4(e and f), after 5 h exposure, the carbon filaments are significantly longer with diameters ranging from 100 - 400 nm and exhibiting a twisted and entangled morphology. After 20 h FL-a_c exposure, most of the surface is covered by filamentous carbon (Fig. 4(g and h)). Some few and small areas are not fully covered by carbon, but these do display short emerging carbon filaments. An example can be seen from the inset in Fig. 4(h), which contains two filaments of ~200 nm diameter and ~400 nm length, each with a catalyst particle at the tip. This demonstrates that the complete sample surface is attacked by carbon formation phenomena leading to metal dusting corrosion.

Our pre-oxidized Inconel 601 alloy hence shows different performance regarding carbon deposition under the different conditions at 750 °C. First, the carbon filaments formed under FL-a_c at 20 bar were usually larger in diameter than those formed under I-a_c at 1 bar. This is in accordance with observations reported by Zeng and Natesan [42]. Then there appears to be less carbon within 2 h under finite low than under infinite carbon activity. However, as the exposure time is prolonged to more than 5 h, this is different; i.e. the carbon filaments formed under finite low carbon activity are longer and more abundant. This indicates that the mechanism is different, with a longer incubation period but more facile growth once it has been initiated under finite low carbon activity.

Raman spectroscopy was used to further investigate the formation of carbon on the surface. The spectra obtained are displayed in Fig. 5(a) for the I-a_c case and 5(b) for the corresponding FL-a_c exposures. All Raman shifts obtained in the range 1000-3000 cm^{-1} can be related to surface carbon, to which Raman is very sensitive. The main order *G band* in the range 1577-1608 cm^{-1} exists for all sp^2 carbon systems, such as amorphous carbon, carbon nanostructures and graphite. It relates to bond stretching of sp^2 pairs only [43]. The other important band is the *D band*, also called "disorder-induced", is found in the range 1326-1328 cm^{-1}. It requires a defect for momentum conservation, which can be anything that breaks the symmetry in the graphene lattice, such as sp^3-defects [44], vacancies [45], grain boundaries [46], or an edge [47]. The *D' band,* defined as a shoulder observed in the range 1600-1610 cm^{-1}, is also dependent on structural disorder. For some cases, the *2D band* (also called G') recorded in the region 2658 cm^{-1} may be very strong. It originates from a second order Raman process related to the in-plane breathing-like mode of the carbon ring, and is hence directly related to the graphitization of the carbon species [48] and especially sensitive to the number of graphene layers [49,50]. In addition to these common bands, one can add the *D + G band* at 2900 cm^{-1} which is defined as a combination scattering peak [51–53]. In terms of carbon structures deposited on a surface, the intensity of G and 2D bands are both related to the number as well as the order of graphene layers [45,46]. As the extent of disorder in the carbon species increases, the Raman intensity increases for the peaks *D*, *D'*, and *D + G* [53,54].

The Raman spectra show that the I- a_c carbon structures have many defects due to the presence of D (1327 cm^{-1}), D' (1607 cm^{-1}), and D + G (2900 cm^{-1}) bands (Fig. 5(a)). These bands are relatively prominent after 1 h as compared to G (1577 cm^{-1}) and 2D (2658 cm^{-1}). However, a G and 2D band intensity increase is predominant during prolonged exposure to 10% CO in Ar (1 bar, I-a_c), from 1 h to 20 h at 750 °C, while the full width at half maximum (FWHM) of both peaks clearly decreases. The D band slightly narrows with longer exposures, while - notably - the D′ band increase ceases when the exposure time reaches 20 h. The D + G band does not increase significantly after 1 h. Both the D and G bands are slightly shifted to lower wave numbers. I_{2D} after 5 h is much stronger than after 1 h and 2 h and extended exposure to 20 h yields another large increase. The I_D/I_G intensity ratios are plotted in Fig. 6, and the ratio for I-a_c is decreasing with exposure time. The overall crystallinity of the carbon formed on the pre-oxidized alloy samples is hence improved by prolonged exposure [22,48]. This implies that, during exposure to CO only, some disordered and amorphous carbon synthesizes first, and more ordered carbon is thereafter formed on top [55].

When it comes to the samples exposed to the simulated syngas (FL-a_c) at 20 bar, the D (1327 cm^{-1}), D' (1607 cm^{-1}), and D + G (2900 cm^{-1}) bands display higher intensity in the case of FL-a_c samples than observed for I- a_c (Fig. 5(b)). Furthermore, the D band narrows with exposure time, and the (relatively small) D′ band also seems to increase slightly. Amorphous carbon is dominated by sp^3 even if some sp^2 bonding coexists (G band) [56]. The abovementioned I_D/I_G ratio (Fig. 6) initially increases strongly, followed by a gradual increase from 5 to 20 h, but always a faster increase in sp^3 hybridization than in sp^2 configuration. The 2D band is not visible for the 1 h exposure but a small, broad peak can be seen after 2 h exposure that only slightly grows until 20 h. This implies that there is no improved crystallinity of the growing carbonaceous deposits. Amorphous carbon is also synthesized first on the pre-oxidized alloy surface during the syngas (FL- a_c) exposure, but what is different compared to the CO (I- a_c) exposure is that disordered carbon

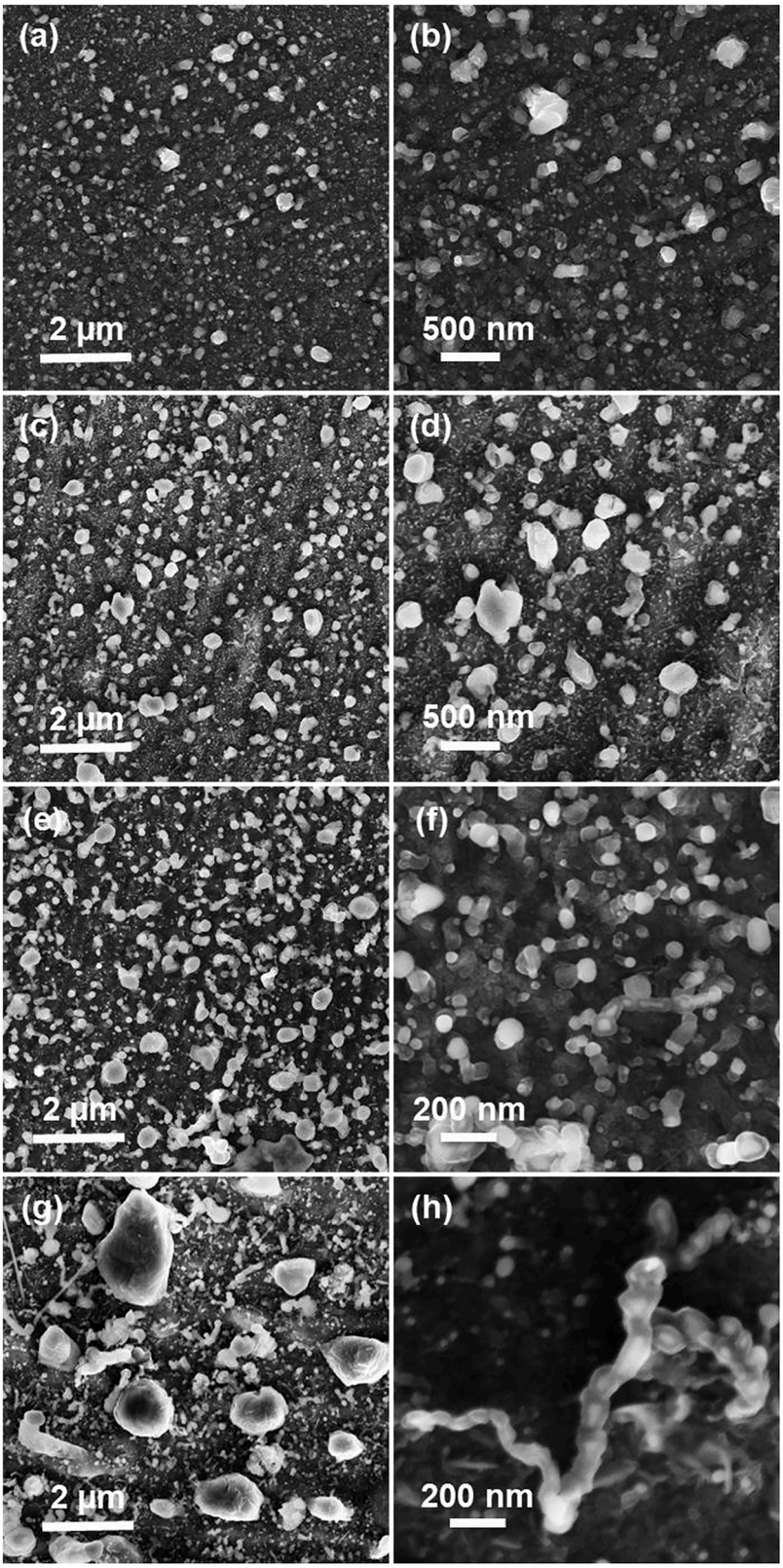

Fig. 3. SEM micrographs at small and large magnification of oxidized Inconel 601 surface after exposure to infinite carbon activity (I- a_c) at 750 °C for (a, b) 1 h; (c, d) 2 h; (e, f) 5 h; (g, h) 20 h. Total pressure 1 bar, 10% CO in Ar.

maintains predominant.

The differences in carbon growth mean that apart from thermodynamic control in the reaction (a_c), the kinetic dependence on temperature and partial pressures of the gaseous reactants also strongly affects the surface carbon deposition. This is in accordance with observations reported by Zhang and Young showing that for a fixed carbon activity ($a_c = 19$) but varying gas composition, both the Boudouard and the CO reduction reactions contributed to carbon deposition. The gasification of

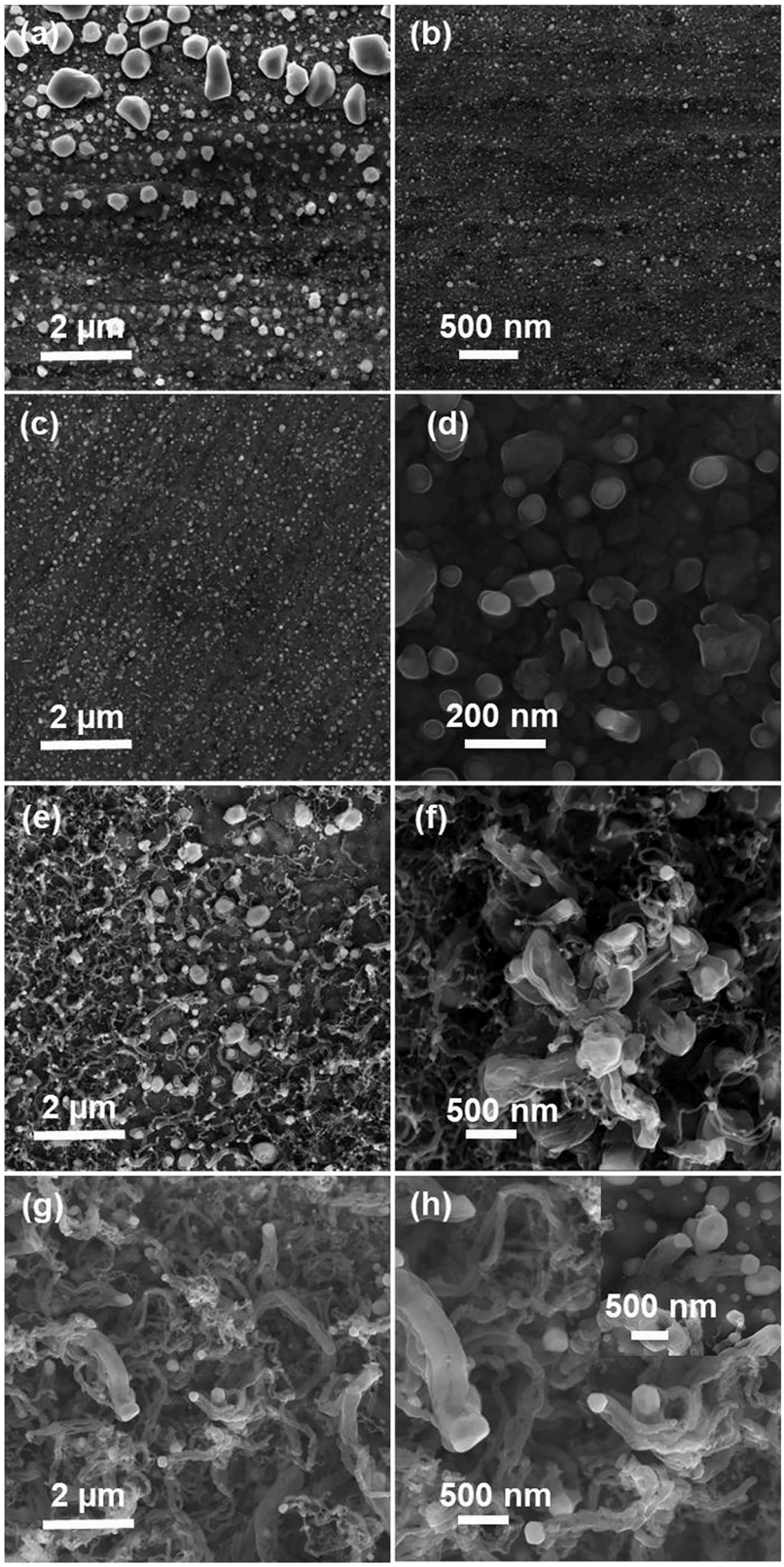

Fig. 4. SEM micrographs at small and large magnification of oxidized Inconel 601 surface after exposure to simulated synthesis gas of finite low carbon activity (FL-a_c), at 750 °C for (a, b) 1 h; (c, d) 2 h; (e, f) 5 h; (g, h) 20 h. Total pressure 20 bar, H_2 (25%), CO (20%), CO_2 (15%), H_2O (10%), Ar (30%).

carbon by hydrogen was important at high hydrogen partial pressures [57]. Zhang et al. also compared exposure to CO/CO_2 (Boudouard) and $H_2/CO/CO_2$ (CO reduction) mixtures for model Fe-Ni alloys as well as 304 steel, and suggest that the faster rate of the latter reaction can lead to higher degrees of carbon supersaturation in the steel [25,58]. CO reduction being kinetically favored over the Boudouard reaction under metal dusting relevant atmospheres is well established [25,58]. However, it remains to be substantiated if H_2-assisted activation of the CO as

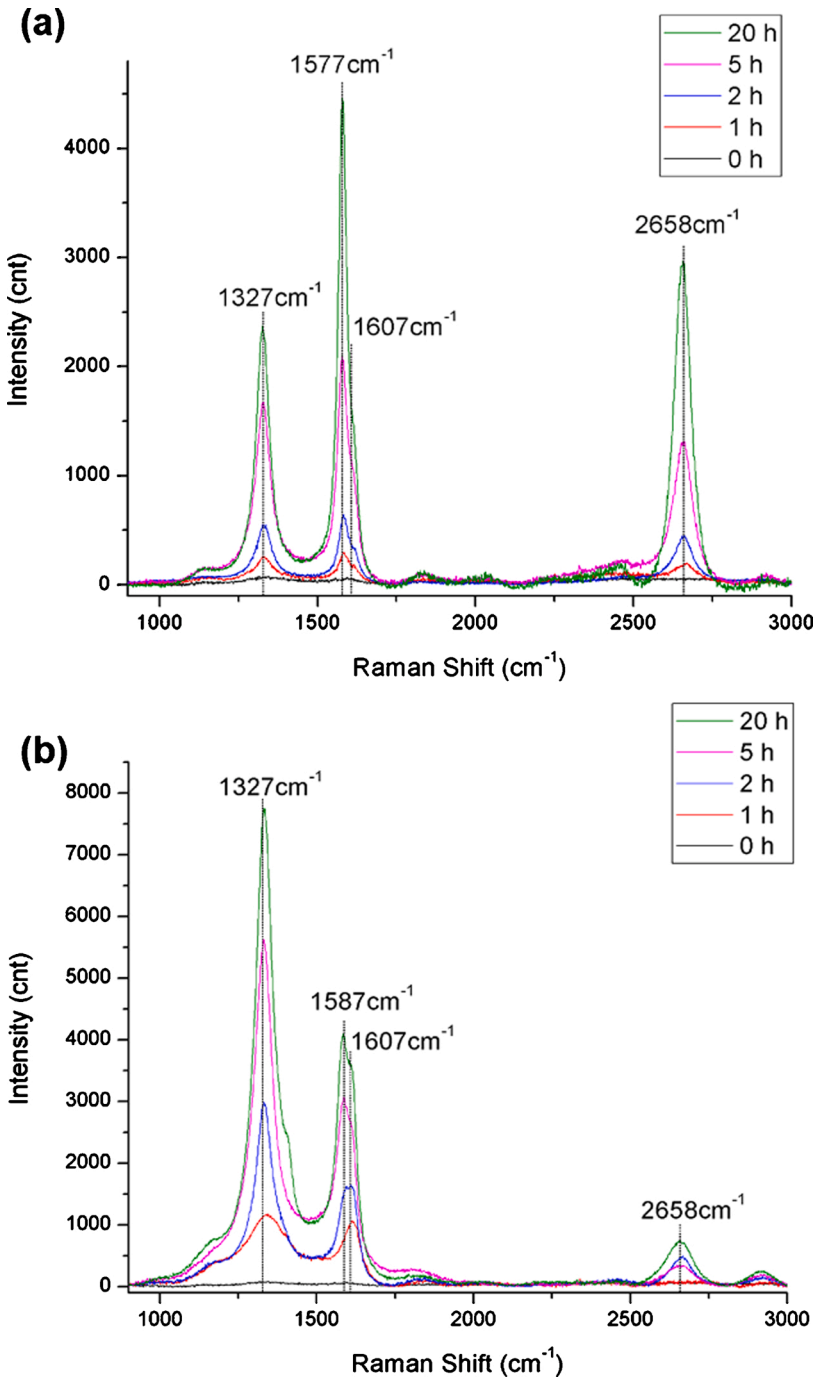

Fig. 5. 1000-3000 cm^{-1} region Raman spectra of oxidized Inconel 601 after exposure to (a) infinite carbon activity (I- a_c) at 750 °C for 0 h, 1 h, 2 h, 5 h and 20 h Total pressure 1 bar, 10% CO in Ar; or (b) simulated synthesis gas of finite low carbon activity (FL- a_c), at 750 °C for 0 h, 1 h, 2 h, 5 h and 20 h. Total pressure 20 bar, H_2 (25%), CO (20%), CO_2 (15%), H_2O (10%), Ar (30%).

known from CO hydrogenation catalysis is important to the nature as well as the rate of the carbon formed in this respect [59,60]. Since the samples qualitatively exhibit contradictory behaviors with respect to the initial carbon formation and the progress with longer exposure, this cannot be concluded from the present work. But the kinetics of carbon deposition is here affected by a gradual structure and composition development of the alloy surface. It is thus worth to investigate the composition and structure of the alloy, as well as changes resulting from the exposures.

3.3. Surface oxide layer development

Fig. 7 compares the XRD patterns of the pre-oxidized Inconel 601 samples after 20 h under the two different metal dusting conditions to the sample oxidized in steam only (also shown in Fig. 1 and discussed above). After exposure under infinite carbon activity, Cr_2O_3 emerges as a new phase in addition to the bulk fcc alloy matrix. In contrast, the major additional phase observed by XRD after exposure to finite low carbon activity is (Ni, Fe, $Cr)_3O_4$ spinel [5]. Neither of these could be confirmed by XRD of the pre-oxidized sample only, but both were present in the thin (40-50 nm) surface layer according to Raman. There has clearly been a development in the oxide structure alongside the carbon

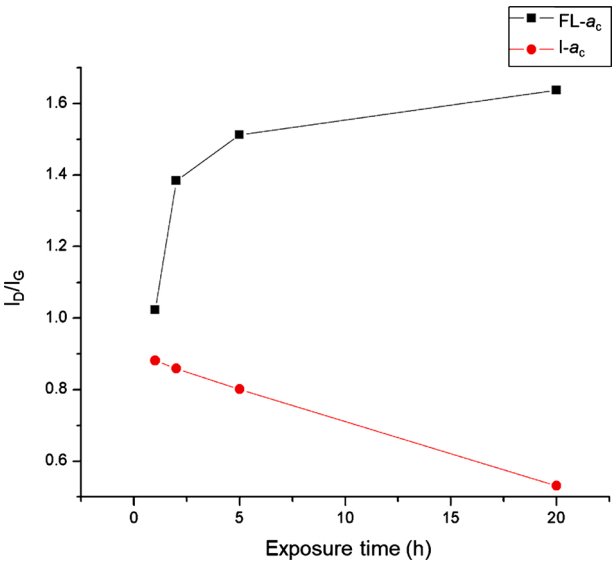

Fig. 6. I_D/I_G intensity ratios of the Raman spectra for oxidized Inconel 601 after exposure to infinite carbon activity (I-a_c) or simulated synthesis gas of finite low carbon activity (FL- a_c) plotted as a function of exposure time.

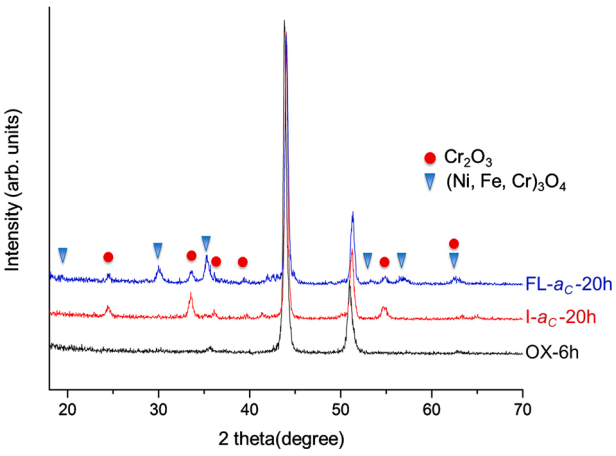

Fig. 7. X-ray diffraction patterns from oxidized Inconel 601 before and after 20 h of exposure to infinite carbon activity (I-a_c) or simulated synthesis gas of finite low carbon activity (FL- a_c).

formation for both exposures. As mentioned before, an adherent Cr_2O_3 scale can protect an alloy from carbon attack. (Ni, Fe, Cr)$_3O_4$ spinel varieties, on the other hand, are not preferred since they are thermodynamically less stable than Cr_2O_3 and can be spalled more easily as a result of stress [61]. Under metal dusting conditions (Ni, Fe, Cr)$_3O_4$ spinel can be partly reduced upon application in low P_{O2} environments containing CO and/or H_2. Carbon can deposit at the surface of Ni and/or Fe metal particles formed upon reduction [24,62,63]. If the higher content of spinel phase after syngas exposure is a signature of continuous formation and decomposition of spinel, it is a possible reason as to why more carbon is formed than under CO in Ar exposure after the initial incubation.

The Raman spectra from the 200-900 cm^{-1} region shown in Fig. 8(a) and (b) present results complementary to the information from XRD. Fig. 8(a) shows that with extended exposure time under I-a_c, the five peaks of Cr_2O_3 (304, 355, 529, 553 and 616 cm^{-1}) [41] increase in intensity while becoming narrower and more symmetric. The spinel peak at 685 cm^{-1} [35], however, does not change much as the exposure time extends from 1 h to 20 h. The Cr_2O_3/spinel peak ratio is hence clearly increasing in parallel with the formation of solid carbon during exposure

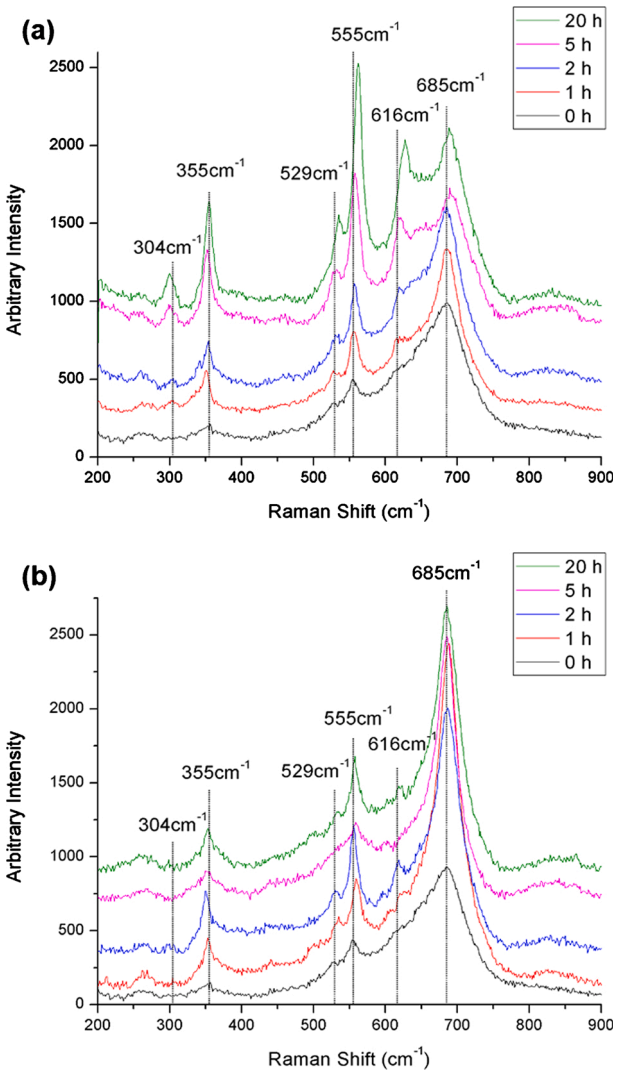

Fig. 8. 200-900 cm^{-1} region Raman spectra of oxidized Inconel 601 after exposure to (a) infinite carbon activity (I- a_c) at 750 °C for 0 h, 1 h, 2 h, 5 h and 20 h Total pressure 1 bar, 10% CO in Ar; or (b) simulated synthesis gas of finite low carbon activity (FL- a_c), at 750 °C for 0 h, 1 h, 2 h, 5 h and 20 h. Total pressure 20 bar, H_2 (25%), CO (20%), CO_2 (15%), H_2O (10%), Ar (30%).

to CO. Formation of Cr_2O_3 from the alloy is also governed by the temperature and the diffusion rate of the Cr cation towards the surface [61], in addition to an effective P_{O2}. In principle, the only sources of oxygen are the oxide phases existing in the surface layer and the oxygen from the CO. The development in the Cr_2O_3 may thus be due to either parallel reduction and oxidation occurring within the oxide or transfer of oxygen to the layer due to CO dissociation at elevated temperature. The latter implies that the Boudouard reaction is not the only reaction proceeding, and that the low effective oxygen partial pressure is sufficient to oxidize Cr [58]. The Raman peaks of both Cr_2O_3 and spinel also show slight shifts towards higher wavenumbers relative to the bands recorded for pure chemicals. This is likely caused by a decrease in interatomic distances [64], i.e. mechanical stress may be present within the oxide [65, 66]. Such a stress may explain why carbon formation proceeds with continued exposure. Even if the amount of Cr_2O_3 increases, the stress causes defects that allow continuously renewed access to Ni, Fe and/or reducible phases thereof.

For the oxidized alloy samples exposed to FL- a_c, peaks from (Ni, Fe, Cr)$_3O_4$ spinel remains dominant throughout the exposure time compared to Cr_2O_3 as can be seen in Fig. 8(b). The Cr_2O_3/spinel peak ratio remains practically constant, and the abovementioned peak shifts

were found for neither the Cr_2O_3 nor the spinel. The slight increase in all peaks parallel to the appearance of the spinel in the XRD pattern after 20 h nevertheless implies development of the oxide. Gunawardana et al. also previously showed by Auger spectrometry an increase in the oxide thickness (~ 500 nm) under same carburizing condition [20]. This implies reduction as well as oxidation schemes different from the infinite carbon activity, CO only, case. The main difference lies in the presence of H_2, H_2O and CO_2, and the overall higher total pressure. Both H_2O and CO_2 can oxidize Cr and Fe and facilitate the formation of $(Ni, Fe, Cr)_3O_4$ spinel on the surface of the alloy [67], while H_2 may play a role in the reduction of both oxides in addition to CO. Higher total pressure of synthesis gas mixtures has in several contributions, accounting for a wide range of alloy compositions, exposure times and progress of the carburization, been found to lead to more severe metal dusting [68–71]. Nishiyama et al. found, that upon exposure of alloy 800H to carbonaceous environments (100 h, CO, H_2, CO_2 and H_2O), the ratio of Cr_2O_3 to spinel type oxides such as $FeCr_2O_4$ decreases with increasing pressure [69]. Also, Madloch et al. reported that both alloy 600 and alloy 800H could form protective chromium oxide on the metal surface under ambient total system pressure (H_2, CO, CO_2, CH_4, H_2O), while high total pressures lead to the formation of spinels such as $MnCr_2O_4$ and/or $FeCr_2O_4$ [68]. A higher rate of formation for these spinels were proposed to induce stress that in turn can deteriorate the protective behavior. Put et al. ran experiments at different total pressures and gas velocities, but similar a_c (H_2, CO, CO_2, CH_4, H_2O/H_2, CO, H_2O), and found that the metal dusting mass loss increases and the average incubation time decreases with pressure for both the HR120 and 800H alloys [70]. Natesan and Zeng also reported that for similar a_c (H_2, CO, CO_2, H_2O/H_2, CO, H_2O), all the 6 different alloys tested showed a decrease in initiation time for metal dusting degradation at higher total pressure [71].

3.4. Cross-section analysis

Three TEM lamellae were prepared by FIB milling from the sample surface after metal dusting corrosion testing, one after 20 h exposure to I-a_c (Figs. 9 and 10) and another two from 2 h (Fig. 11) and 20 h (Fig. 12) exposure to FL-a_c conditions. The red line in the SEM image of Fig. 9(a) shows the location of the cross-section I-a_c TEM lamella. It extends through a region in the center with less carbon, seemingly a surface of different characteristics than the surroundings. The cross-section SEM image of the lamella with carbon protection layer after milling is shown in Fig. 9(b), and this is a good example of a TEM lamella where ion-beam damage has been avoided. The carbon filaments on the surface and the grain boundaries underneath are not very clear due to the low magnification. Low-angle annular dark-field scanning transmission electron microscopy (LAADF STEM) was therefore employed to obtain more details of the region within the red square in Fig. 9(b), as shown in Fig. 9 (c). Carbon filaments with metal particles at the tip can be observed on the top of the lamella within the carbon protection layer. The diameter of these carbon filaments varies over a broad range. Grain boundaries are indicated by blue lines in the figure. It can be seen that the mid-section grain is resulting from a straight grain boundary that goes from the bulk towards the surface, an then bends to continue relatively parallel to the surface (blue solid line in figure) before extending to the surface on the right. Thus, the center area with less carbon is associated with a relatively small and shallow part of a larger grain.

Chemical composition mapping by simultaneous EDS and EELS was performed from the two regions indicated by red rectangles in Fig. 9(c). The element maps are displayed in Fig. 10(a) and (b) for the right and left of these two regions, respectively. The elementary maps for O, Cr and Mn in Fig. 10(a) confirm that a thin Cr-rich oxide covers the alloy surface. As to be expected, the bulk matrix under the surface oxide layer is rich in Ni and Fe. The shallow grain boundary is located in the middle of Fig. 10(a) and striking differences can be observed between each side of this grain boundary. Firstly, while the shallow part of the grain to the left appears depleted in Cr, Cr-rich oxide precipitates can be observed inside the grain on the right. Mn generally tends to be accompanied with the Cr. Small Ni and Fe rich particles are clearly also present on top of the oxide, and seemingly more abundant to the right than to the left. Al and Ti were found as oxides mainly at the interface between the bulk alloy and the Cr-rich scale, and it is worth to note that the Al and Ti EDS signal is stronger on the left side than on the right side of the grain boundary (See Fig. S2 in the Supporting Information). Slight Si enrichment can also be observed at the interface between the alloy and the oxide scale.

Due to insufficient EDS signal from carbon, EELS was applied for the C-mapping. The carbon protection layer deposited during FIB preparation dominates the C element map. However, the carbon located in the filaments can still be distinguished from the amorphous carbon protection layer. The carbon deposits consist of filaments of various length and thickness, and the observation that there is less carbon at the surface of the shallow grain is apparent also in the cross-section TEM lamella. The

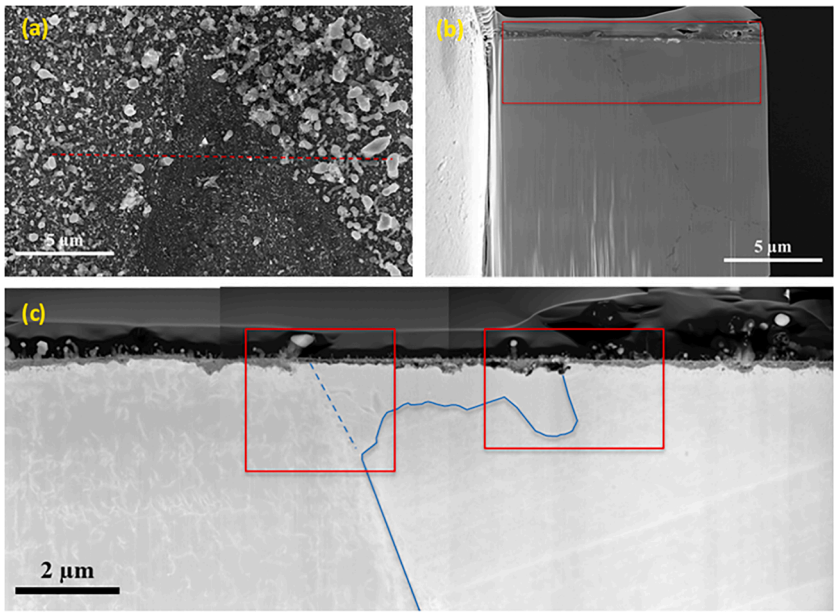

Fig. 9. Preparation of TEM lamella by FIB milling from oxidized Inconel 601 after exposure to infinite carbon activity (I- a_c) at 750 °C for 20 h. (a) SEM surface view of the region from where the FIB sample was selected. (b) SEM image of the cross-section TEM lamella, region indicated in red square is further analyzed by LAADF STEM. A thin protection layer of C was deposited on the alloy surface before ion milling, and can be observed in upper part of the images. (c) LAADF STEM image of the TEM lamella with solid line indicating grain boundary and dashed line indicating the extension line of this grain boundary into the grain matrix and towards the surface. The two red squares indicate regions further analyzed by EDS and EELS (Fig. 10).

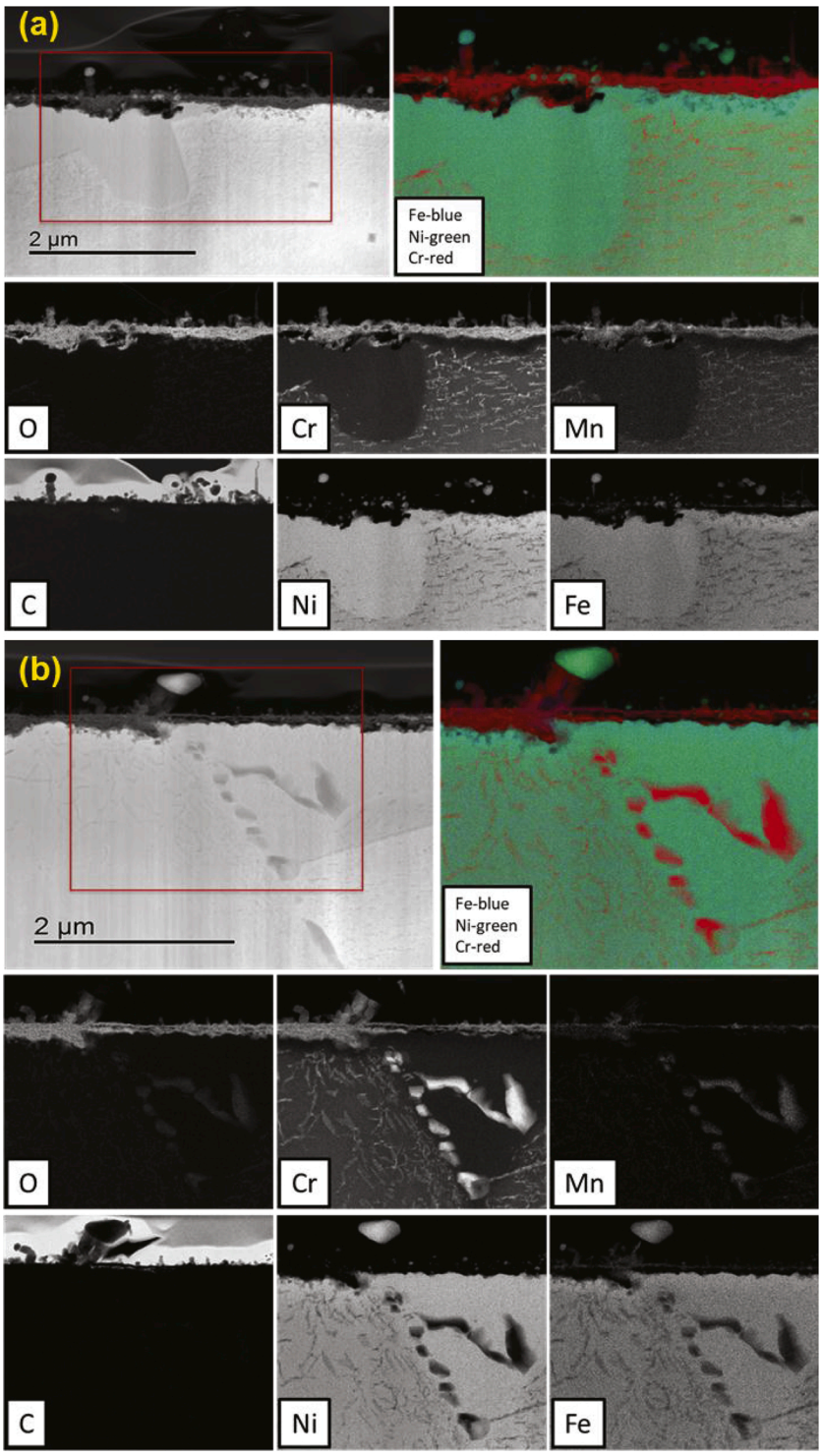

Fig. 10. STEM images, EELS (C signal) and EDS (other signals) element mapping, and RGB element merge of selected regions of TEM lamella milled by FIB from oxidized Inconel 601 sample after exposure to infinite carbon activity (I- a_c) at 750 °C for 20 h; (a) right region and (b) left region indicated by the red squares in Fig. 9.

Ni and Fe rich metal nanoparticles are clearly associated with the tip of the carbon filaments. It should also be noted that significant O, Cr, Mn and a little bit of Fe can be observed inside the carbon filaments. The carbon growth could hence be related to a partial decomposition of (Ni, Fe, Cr)$_3$O$_4$ spinel phases present after steam oxidation pre-treatment, which then serve as "impure" catalyst particles for the first carbon deposition. Further CO exposure makes the filaments grow and lifts the catalyst particles up while simultaneously leaving behind "impurities" along the core of the filaments to render the particle at the tip as an increasingly pure Ni-Fe alloy. This suggests that (Ni, Fe, Cr)$_3$O$_4$ spinel is not formed in reaction with CO only and may explain why the overall crystallinity of the carbon formed under prolonged exposures to I-a_c is improved as discussed above.

Fig. 10(b) only covers a short part of the grain boundary, in the lower right corner of this region. However, it is interesting to see that some Cr-rich oxide precipitates form a line (indicated as dash line in Fig. 9(c))

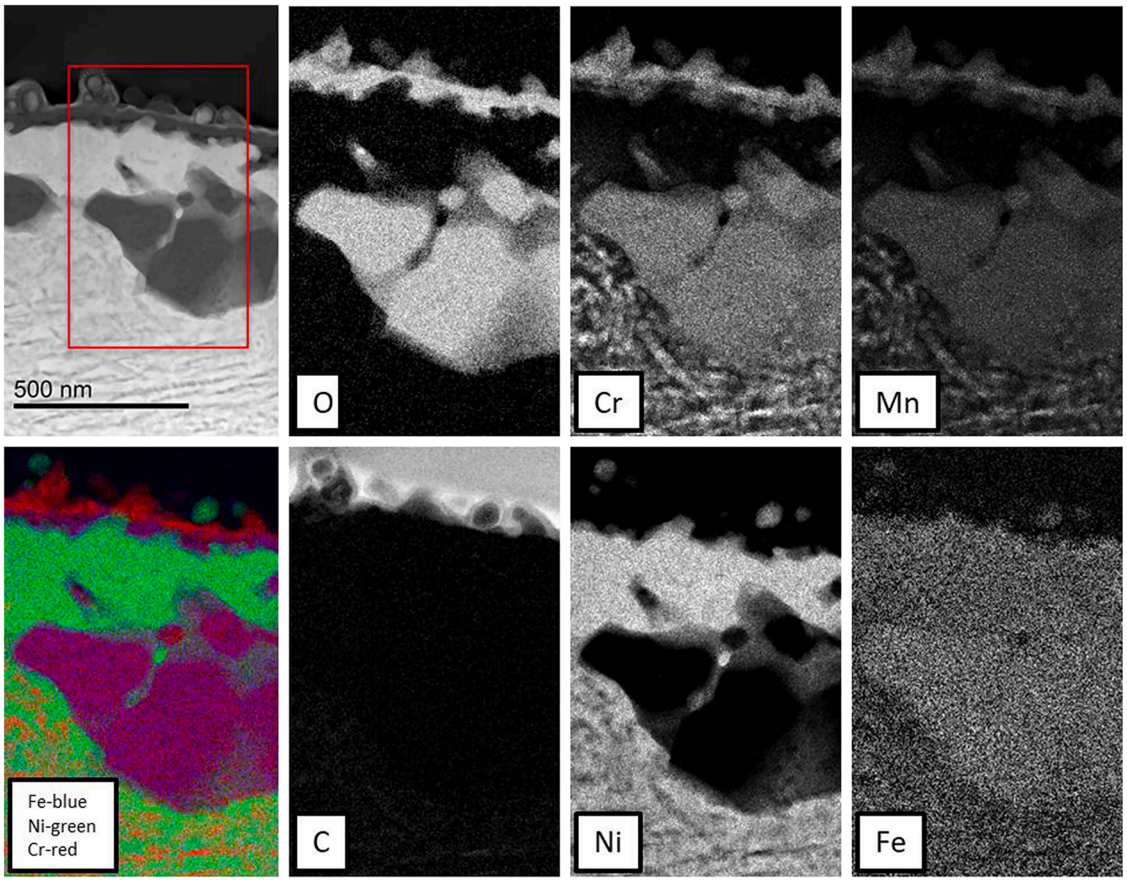

Fig. 11. STEM images, EELS (C and Fe signals) and EDS (other signals) element mapping, and RGB element merge of selected regions of TEM lamella milled by FIB from oxidized Inconel 601 sample after exposure to finite low carbon activity (FL- a_c), at 750 °C for 2 h. A thin protection layer of C was deposited on the alloy surface before ion milling, and can be observed as background in the C map.

exactly at the extension of the straight grain boundary underneath. On the left side of this "precipitate boundary" the surface Cr-oxide layer is relatively thick (100-290 nm) and underneath Cr-rich oxide precipitates are found homogeneously dispersed within the Ni-Fe matrix. On the right side, on the other hand, the surface oxide layer is thinner (70-100 nm) and underneath the internal Cr-rich oxide precipitates are fewer, larger and form a long meandering strip. Surrounding the Cr-rich precipitates, the shallow part of the grain has become depleted in Cr. All of this indicates that the grain boundary has played a role in the transport of Cr towards the surface, supporting the notion that grain boundaries are channels for Cr [72].

As could be inferred from the SEM images in Fig. 4, the amount of carbonaceous deposits after exposure to the finite carbon activity, simulated syngas (FL-a_c) was much higher after 20 h than for the corresponding CO only exposure. However, the 2 h FL-a_c exposure presented a surface with similar appearance (Fig. 4(c) and (d)) as the 20 h I-a_c. Thus, a TEM lamella was prepared from the former by FIB milling. Fig. 11 shows chemical composition mapping by EDS and EELS. The element maps of O, Cr, and Mn confirm that a Cr-rich oxide covers the alloy surface also here; ~40-96 nm thick as observed from the dark field STEM and including Mn. Metal particles with only a few layers of carbon are observed on top of the oxide. These catalyst particles are rich in Ni but contain also some Fe. Close inspection reveals that they are also actually wrapped by a thin layer of Cr-rich oxide, and this could be the signature of a decomposed spinel phase (See Fig. S3 in the Supporting Information). Below the surface oxide layer, large oxide precipitates can be observed, reaching ~550 nm into the matrix, which are rich in Cr and may contain some Fe. More dispersed Cr-rich oxide precipitates are found below the large precipitates, but not above them. Similar to the sample in Fig. 10, slight Si, Al and Ti enrichment can be observed at the alloy and oxide scale interface (See Fig. S4 in the Supporting Information).

To reach the oxide layer of the alloy and enable further sample preparation, the carbon and corrosion products after 20 h exposure to the finite carbon activity, simulated syngas (FL-a_c) were removed by ultrasonic agitation in acetone. Pt deposition to protect the surface layer during ion milling was applied before TEM lamella preparation. Fig. 12 shows a TEM lamella on which a corrosion pit has developed. EDS based element maps from the region labelled by the red frame in the dark field STEM image are also shown. These element maps show that oxygen has penetrated much deeper into the alloy matrix compared to the alloy samples exposed to I-a_c, yielding a 430-830 nm thick oxide layer. It can be observed from the dark field STEM image that the surface oxide consists of two layers: A seemingly porous, ~ 170 nm dark STEM contrast layer on the top with a thicker ~260 - 660 nm discontinuous layer below. This thick layer probably results from continued formation of Cr-rich oxide precipitates such as those observed from Fig. 11. O, Cr and Mn are overlapped within the entire oxide layer. Filamentous carbon within the pit indicates that strongly attached carbon filaments were not removed by the ultrasonic agitation and preserved during FIB milling. Carbon is also found progressed into the topmost oxide, and this has previously also been substantiated from Auger depth profiles from same exposures [20]. The Ni and Fe maps show that metallic Ni-Fe phases occupy the interstice within the discontinuous oxide. Ni and Fe rich nanoparticles are also observed in the pit, which indicate that these particles serve as catalysts for carbon deposition. The original oxide scale must have been destroyed in the pitting area; however, a new, thin less protective oxide has formed at the bottom of the pit with similar

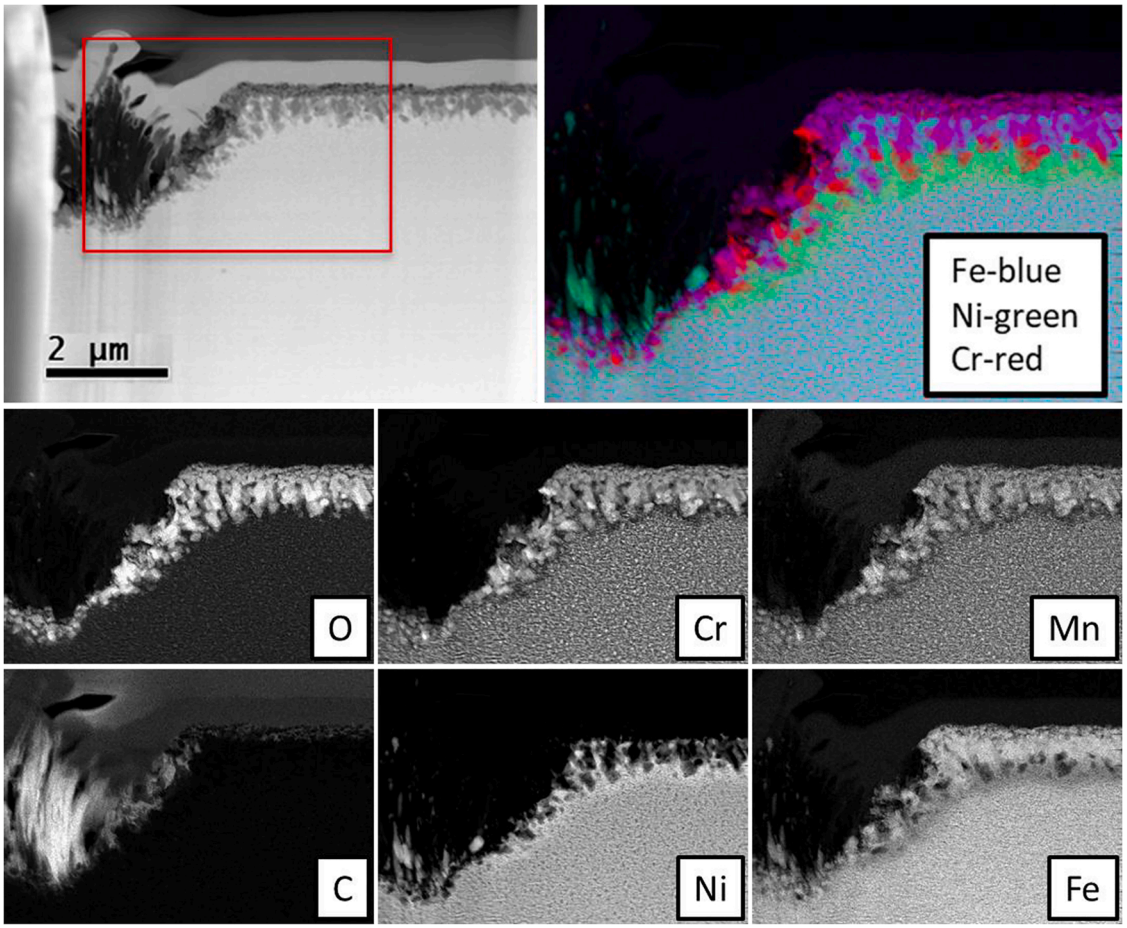

Fig. 12. STEM image, EDS element mapping and RGB element merge of region selected from TEM lamella milled by FIB from oxidized Inconel 601 after exposure to simulated synthesis gas of finite low carbon activity (FL- a_c), at 750 °C for 20 h and subsequently subjects to ultrasonic cleaning. A thin protection layer of Pt was deposited on the alloy surface before ion milling that can be observed in the upper left image.

composition outside of the pit. A similar observation was also made by Zhang et al [58]. When the protective chromia was lost, inward diffusion of O resulted in the formation of less protective internal precipitates such as $FeCr_2O_4$ or other spinel types. It should be noted that the Pt protection layer gives an enhanced bremsstrahlung background signal compared to the rest of the mapped region that shows up as an artefact in the Al, Ti and Si maps (See Fig. S5 in the Supporting Information). Nevertheless, Al, and possibly also Ti and Si signals are distinguishable at the interface between the bulk alloy and the oxide scale, but part of the Al is also dispersed within the oxide layer, more dispersed than for the sample exposed to I- a_c.

By comparing Figs. 10 and 12, we can see that oxide scale developed under I-a_c is significantly thinner (~70-290 nm) than that developed under FL-a_c (~430-830 nm). The central part of the TEM lamella where the oxide is thinnest produced the least amount of carbon filaments. This indicates that a protective oxide scale against metal dusting corrosion is not necessarily thick. Presumably, a dense, defect free and chemical stable oxide is desired. The central area showed in Fig. 9(c), located between a grain boundary and a dashed line which function similar to a grain boundary, represents a local fine-grained structure. The impact of a fine grain-structure thus appears to have been rapid formation of a thin, but comparatively resistant surface oxide. A fine-grained structure is found to provide diffusion paths along grain boundaries, sub-boundaries and dislocations, resulting in an enhanced Cr diffusivity that enables a faster formation of a protective, Cr-rich oxide in the surface region [6,73]. Grain boundaries are also associated with inter-phase energy, hence yielding an overall more reactive phase [74–76]. The relatively dense Al oxide scale beneath may also play an important role in mitigating metal dusting attack [5].

Finally, the kinetics and thermodynamics of the oxide formation under FL-a_c produces a different oxide than under I-a_c. The presence of steam and CO_2 and significantly higher partial pressures of the oxygen species ($CO/H_2O/CO_2$) yields deeper oxidation in parallel with the carbon formation but seems to favor spinel over Cr oxide. This (Ni, Fe, $Cr)_3O_4$ spinel is subsequently reduced and thereby more prone to participate in continued formation of highly defected carbon. It remains to fully explain the formation of Cr_2O_3 under CO exposure only (I-a_c) and to which extent it eventually can inhibit further progress of the carbon formation. It could be that a low efficient oxygen partial pressure is beneficial in terms of allowing sufficient transport of Cr for the reaction. Likewise, the key mechanism for spinel formation should be established, but interplay between Cr transport and the kinetics of reducing (H_2/CO) and oxidizing reactions (H_2O/CO_2) likely is important.

4. Conclusion

Nickel-based alloy (Inconel 601) samples have been pre-oxidized in 10% steam in Ar at 540 for 6 h before exposure to two different metal dusting conditions at 750 °C. We have shown that by varying the exposure times over relatively short exposures, we may capture the initiation and progress of carbon formation on alloy surfaces that eventually leads to metal dusting. The carbon deposition is clearly a function of the gas composition during exposure. After 20 h, less carbon has formed under 10% CO in Ar (1 bar), i.e infinite carbon activity (I-a_c), than under synthesis gas with finite low carbon activity (FL-a_c; 25% H_2,

20% CO, 15% CO_2, 10% H_2O, and 30%Ar, 20 bar). However, the formation of carbon under FL-a_c exhibits a longer incubation period than under I-a_c, but more facile growth after the first 1-2 h. SEM confirms the formation of filamentous carbon for both exposures, albeit overall larger diameters with H, CO_2 and H_2O present in the mixture. Moreover, Raman spectroscopy reveals significant differences in the nature of the carbon formed. With only CO reacting (I-a_c), more ordered carbon develops as the exposure time increases, while this is not case under synthesis gas. Combined, this points to a difference the catalytic reaction mechanism and kinetics on the surface.

In addition, XRD, Raman and TEM characterization reveal that the surface oxide layer formed on Inconel 601 develops very differently under the two metal dusting conditions applied. Cr_2O_3 develops as a thin surface oxide scale layer under exposure to CO in Ar. A more fine-grain structure present near the surface in certain regions on this sample is found important in terms of rapidly supplying Cr, Mn and Al to the surface under elevated temperature to form a better protective layer and thereby slowing the metal dusting corrosion. TEM analysis captured another interesting evolution under I-a_c, which suggests "purification" of the catalyst particles along with carbon filaments growth as a possible reason for the improved overall crystallinity of the carbon formed during prolonged exposure. In presence of synthesis gas (FL-a_c), oxidation proceeds within a larger part of the near-surface region, but results to a higher extent in (Ni, Fe, Cr)$_3O_4$ spinel formation. We suggest that this phase continuously forms and reduces to new carbon formation catalyst (Ni, Fe) particles that nucleate the formation of more, less ordered carbon.

CRediT authorship contribution statement

Xiaoyang Guo: Conceptualization, Validation, Formal analysis, Investigation, Data curation, Writing - original draft, Writing - review & editing, Visualization. **Estelle Vanhaecke:** Methodology, Validation, Formal analysis, Investigation, Data curation, Writing - original draft, Visualization. **Per Erik Vullum:** Methodology, Validation, Formal analysis, Investigation, Data curation, Writing - original draft, Visualization. **Jianyu Ma:** Validation, Investigation. **P.V. Daham S. Gunawardana:** Methodology, Investigation. **John C. Walmsley:** Conceptualization, Methodology, Formal analysis, Investigation. **De Chen:** Conceptualization, Project administration, Funding acquisition. **Hilde J. Venvik:** Conceptualization, Methodology, Writing - original draft, Writing - review & editing, Supervision, Funding acquisition.

Declaration of Competing Interest

The authors declare that they have no known competing financial interests or personal relationships that could have appeared to influence the work reported in this paper.

Acknowledgements

The financial support of Research Council of Norway under the GASSMAKS research program (Contract No. 233869/E30) is gratefully acknowledged. The TEM work was carried out on NORTEM infrastructure, Grant 197405, TEM Gemini Centre, Norwegian University of Science and Technology (NTNU), Norway. The Research Council of Norway is acknowledged for the support to the Norwegian Micro- and Nano-Fabrication Facility, NorFab, project number 245963/F50.

Appendix A. Supplementary data

Supplementary material related to this article can be found, in the online version, at doi:https://doi.org/10.1016/j.cattod.2020.04.029.

References

[1] M. Holland, H. De Bruyn, Metal dusting failures in methane reforming plant, International journal of pressure vessels and piping 66 (1–3) (1996) 125–133.
[2] A.B. Tomkings, T. Lant, Operating Experience of Metal Dusting Failures, CORROSION 2001 (2001).
[3] S. Kaewkumsai, W. Khonraeng, N. Sathirachinda, High temperature failure of natural gas feed burner pipe, Engineering Failure Analysis 27 (2013) 74–83, https://doi.org/10.1016/j.engfailanal.2012.08.004.
[4] J. Orlikowski, A. Jazdzewska, K. Darowicki, J. Karczewski, J. Dampc, R. Gospos, Metal dusting phenomena of 501 AISI furnace tubes in refinery fractional distillation unit, Engineering Failure Analysis 91 (2018) 108–114.
[5] Z. Zeng, K. Natesan, M. Grimsditch, Effect of oxide scale compositions on metal dusting corrosion of Fe-based alloys, Corrosion 60 (7) (2004) 632–642.
[6] H. Grabke, E. Muller-Lorenz, S. Strauss, E. Pippel, J. Woltersdorf, Effects of grain size, cold working, and surface finish on the metal-dusting resistance of steels, Oxid. Met. 50 (3) (1998) 241–254.
[7] C. Toh, P. Munroe, D. Young, Metal dusting of Fe–Cr and Fe–Ni–Cr alloys under cyclic conditions, Oxid. Met. 58 (1–2) (2002) 1–21.
[8] R. Lobnig, H. Schmidt, K. Hennesen, H. Grabke, Diffusion of cations in chromia layers grown on iron-base alloys, Oxid. Met. 37 (1–2) (1992) 81–93.
[9] H. Li, W. Chen, High temperature carburization behaviour of Mn–Cr–O spinel oxides with varied concentrations of manganese, Corros. Sci. 53 (6) (2011) 2097–2105.
[10] H. Li, W. Chen, Stability of MnCr2O4 spinel and Cr2O3 in high temperature carbonaceous environments with varied oxygen partial pressures, Corros. Sci. 52 (7) (2010) 2481–2488.
[11] H. Li, Y. Zheng, L.W. Benum, M. Oballa, W. Chen, Carburization behaviour of Mn–Cr–O spinel in high temperature hydrocarbon cracking environment, Corros. Sci. 51 (10) (2009) 2336–2341.
[12] T.A. Ramanarayanan, C. Chun, Metal dusting resistant alloys, ed: Google Patents, 2004.
[13] B. Bao, J. Liu, H. Xu, B. Liu, W. Zhang, Inhibitory effect of MnCr 2 O 4 spinel coating on coke formation during light naphtha thermal cracking, RSC Advances 6 (73) (2016) 68934–68941.
[14] R. Hochman, The fundamentals of metal dusting, in: API Division of Refining Proc, 46, 1966, p. 331.
[15] H. Grabke, R. Krajak, E. Müller-Lorenz, Metal dusting of high temperature alloys, Mater. Corros. 44 (3) (1993) 89–97.
[16] H. Grabke, R. Krajak, E. Müller-Lorenz, S. Strauß, Metal dusting of nickel-base alloys, Mater. Corros. 47 (9) (1996) 495–504.
[17] C. Chun, T. Ramanarayanan, J. Mumford, Relationship between coking and metal dusting, Mater. Corros. 50 (11) (1999) 634–639.
[18] H. Grabke, R. Krajak, J.N. Paz, On the mechanism of catastrophic carburization: 'metal dusting', Corros. Sci. 35 (5–8) (1993) 1141–1150.
[19] P. Szakalos, R. Pettersson, S. Hertzman, An active corrosion mechanism for metal dusting on 304L stainless steel, Corros. Sci. 44 (10) (2002) 2253–2270.
[20] P.D.S. Gunawardana, T.T.M. Nguyen, J.C. Walmsley, H.J. Venvik, Initiation of metal dusting corrosion in conversion of natural gas to syngas studied under industrially relevant conditions, Industrial & Engineering Chemistry Research 53 (5) (2013) 1794–1803.
[21] H. Grabke, Thermodynamics, mechanisms and kinetics of metal dusting, Mater. Corros. 49 (5) (1998) 303–308.
[22] Z. Zeng, K. Natesan, V.A. Maroni, Investigation of Metal-Dusting Mechanism in Fe-Base Alloys Using Raman Spectroscopy, X-Ray Diffraction, and Electron Microscopy, Oxid. Met. 58 (1/2) (2002) 24.
[23] H. Grabke, M. Schütze, Corrosion by Carbon and Nitrogen: Metal Dusting, Carburisation and Nitridation, Elsevier, 2014.
[24] D.J. Young, J. Zhang, C. Geers, M. Schütze, Recent advances in understanding metal dusting: A review, Mater. Corros. 62 (1) (2011) 7–28, https://doi.org/10.1002/maco.201005675.
[25] J. Zhang, D.J. Young, Coking and dusting of Fe–Ni alloys in CO–H2–H2O gas mixtures, Oxid. Met. 70 (3–4) (2008) 189–211.
[26] H.J. Grabke, E.M. Müller-Lorenz, B. Eltester, M. Lucas, D. Monceau, Resistance of 9–20% Cr-steels against metal dusting, steel research international 68 (4) (1997) 179–185.
[27] S. Strauß, R. Krajak, H. Grabke, Coking by metal dusting of nickel-base alloys, Mater. Corros. 50 (11) (1999) 622–627.
[28] D.L. Klarstom, L.D. Paul, H.J. Grabke, The metal dusting behavior of several high temperature nickel based alloys, in: CORROSION 2001, NACE International, 2001.
[29] Y. NISHIYAMA, K. MORIGUCHI, H. OKADA, T. OSUKI, S. KURIHARA, Development of Metal Dusting Resistant Alloy for Synthesis Gas Production Plants. NIPPON STEEL & SUMITOMO METAL TECHNICAL REPORT, 2015.
[30] A.R.-V. Put, K.A. Unocic, M.P. Brady, B.A. Pint, Performance of chromia-and alumina-forming Fe-and Ni-base alloys exposed to metal dusting environments: The effect of water vapor and temperature, Corros. Sci. 92 (2015) 58–68.
[31] H. Stahl, G. Smith, S. Wastiaux, Strain-age cracking of alloy 601 tubes at 600° C, Practical failure analysis 1 (1) (2001) 51–54.
[32] C.H. Toh, P.R. Munroe, D.J. Young, K. Foger, High temperature carbon corrosion in solid oxide fuel cells, Mater. High Temp. 20 (2) (2003) 129–136, https://doi.org/10.1179/mht.2003.016.
[33] F. Mulaudzi, L. Cornish, G. Slabbert, M. Papo, J. Zhang, A study of metal dusting corrosion on Fe-and Ni-based alloys, Journal of the Southern African Institute of Mining and Metallurgy 113 (2) (2013) 121–128.

[34] C.M. Chun, T.A. Ramanarayanan, Metal dusting resistant alumina forming coatings for syngas production, Corros. Sci. 51 (11) (2009) 2770–2776, https://doi.org/10.1016/j.corsci.2009.08.011.
[35] Z. Zeng, K. Natesan, Relationship of carbon crystallization to the metal-dusting mechanism of nickel, Chem. Mater. 15 (4) (2003) 872–878.
[36] Y. Nishiyama, H. Okada, T. Osuki, S. Kurihara, H. Ogawa, Improved metal dusting resistance of new sumitomo 696 ni-base alloy for synthesis gas environments, Nitrogen+ Syngas 2011 International Conference (2011) 129–138.
[37] J.C. Walmsley, J.Z. Albertsen, J. Friis, R.H. Mathiesen, The evolution and oxidation of carbides in an Alloy 601 exposed to long term high temperature corrosion conditions, Corros. Sci. 52 (12) (2010) 4001–4010, https://doi.org/10.1016/j.corsci.2010.08.015.
[38] P. Gunawardana, H. Venvik, J. Walmsley, Investigation of the initial stage of metal dusting corrosion in the conversion of natural gas to synthesis gas, in: CORROSION 2013, NACE International, 2013.
[39] P. Gunawardana, J. Walmsley, A. Holmen, D. Chen, H.J. Venvik, Metal dusting corrosion initiation in conversion of natural gas to synthesis gas, Energy Procedia 26 (2012) 125–134.
[40] P. Gunawardana, Carbon formation phenomena and the initial stage of metal dusting corrosion–an experimental investigation, 2014.
[41] D. Thierry, et al., In-Situ Raman Spectroscopy Combined with X-Ray Photoelectron Spectroscopy and Nuclear Microanalysis for Studies of Anodic Corrosion Film Formation on Fe-Cr Single Crystals, J. Electrochem. Soc. 135 (2) (1988) 305–310.
[42] Z. Zeng, K. Natesan, Relationship between the growth of carbon nanofilaments and metal dusting corrosion, Chem. Mater. 17 (14) (2005) 3794–3801.
[43] M. Tamor, W. Vassell, "Raman "fingerprinting" of amorphous carbon films, J. Appl. Phys. 76 (6) (1994) 3823–3830.
[44] A. Eckmann, et al., Probing the nature of defects in graphene by Raman spectroscopy, Nano Lett. 12 (8) (2012) 3925–3930.
[45] M.M. Lucchese, et al., Quantifying ion-induced defects and Raman relaxation length in graphene, Carbon 48 (5) (2010) 1592–1597.
[46] L.G. Cançado, et al., Quantifying defects in graphene via Raman spectroscopy at different excitation energies, Nano Lett. 11 (8) (2011) 3190–3196.
[47] L. Cancado, M. Pimenta, B. Neves, M. Dantas, A. Jorio, Influence of the atomic structure on the Raman spectra of graphite edges, Phys. Rev. Lett. 93 (24) (2004) 247401.
[48] Y. Sato, M. Kamo, N. Setaka, Raman spectra of carbons at 2600–3300 cm− 1 region, Carbon 16 (4) (1978) 279–280.
[49] J. Park, A. Reina, R. Saito, J. Kong, G. Dresselhaus, M. Dresselhaus, G′ band Raman spectra of single, double and triple layer graphene, Carbon 47 (5) (2009) 1303–1310.
[50] Z. Luo, C. Cong, J. Zhang, Q. Xiong, T. Yu, The origin of sub-bands in the Raman D-band of graphene, Carbon 50 (11) (2012) 4252–4258.
[51] M. Pimenta, G. Dresselhaus, M.S. Dresselhaus, L. Cancado, A. Jorio, R. Saito, Studying disorder in graphite-based systems by Raman spectroscopy, PCCP 9 (11) (2007) 1276–1290.
[52] A.C. Ferrari, D.M. Basko, Raman spectroscopy as a versatile tool for studying the properties of graphene, Nat Nanotechnol 8 (April (4)) (2013) 235–246, https://doi.org/10.1038/nnano.2013.46.
[53] I. Childres, L.A. Jauregui, W. Park, H. Cao, Y.P. Chen, Raman spectroscopy of graphene and related materials, New developments in photon and materials research 1 (2013).
[54] R. Saito, M. Hofmann, G. Dresselhaus, A. Jorio, M. Dresselhaus, Raman spectroscopy of graphene and carbon nanotubes, Advances in Physics 60 (3) (2011) 413–550.
[55] X. Guo, P. Gunawardana, D. Chen, E. Vanhaecke, H. Venvik, J. Walmsley, Investigation of Metal Dusting Corrosion Process over UNS N08800 Alloy, in: CORROSION 2017, NACE International, 2017.
[56] P.K. Chu, L. Li, Characterization of amorphous and nanocrystalline carbon films, Materials Chemistry and Physics 96 (2–3) (2006) 253–277.
[57] J. Zhang, D.J. Young, Kinetics and mechanisms of nickel metal dusting I. Kinetics and morphology, Corros. Sci. 49 (3) (2007) 1496–1512.
[58] J. Zhang, K. Boddington, D.J. Young, Oxidation, carburisation and metal dusting of 304 stainless steel in CO/CO2 and CO/H2/H2O gas mixtures, Corros. Sci. 50 (11) (2008) 3107–3115, https://doi.org/10.1016/j.corsci.2008.08.017.
[59] M. Ojeda, R. Nabar, A.U. Nilekar, A. Ishikawa, M. Mavrikakis, E. Iglesia, CO activation pathways and the mechanism of Fischer–Tropsch synthesis, J. Catal. 272 (2) (2010) 287–297.
[60] M. Ojeda, A. Li, R. Nabar, A.U. Nilekar, M. Mavrikakis, E. Iglesia, Kinetically relevant steps and H2/D2 isotope effects in Fischer− Tropsch synthesis on Fe and Co catalysts, The Journal of Physical Chemistry C 114 (46) (2010) 19761–19770.
[61] M.W. Edwards, N.S. McIntyre, Gas Phase Initial Oxidation of Incoloy 800 Surfaces, Oxid. Met. 79 (1–2) (2013) 179–200.
[62] H. Grabke, I. Wolf, Carburization and oxidation, Materials Science and Engineering 87 (1987) 23–33.
[63] M. Harper, M. Ducasse, D. Young, Cyclic oxidation plus carburization of heat-resistant alloys, Corrosion 51 (3) (1995) 191–200.
[64] J. Mougin, T. Le Bihan, G. Lucazeau, High-pressure study of Cr 2 O 3 obtained by high-temperature oxidation by X-ray diffraction and Raman spectroscopy, J. Phys. Chem. Solids 62 (3) (2001) 553–563.
[65] K. Kitamura, Y. Nishiyama, N. Otsuka, T. Kudo, In Situ Growth-Stress Measurement of Cr2O3 Scale Formed on Stainless Steels by Raman Spectroscopy, Materials science forum 522 (2006) 489–496. Trans Tech Publ.
[66] J. Mougin, N. Rosman, G. Lucazeau, A. Galerie, In situ Raman monitoring of chromium oxide scale growth for stress determination, Journal of Raman Spectroscopy 32 (9) (2001) 739–744.
[67] L. Martinelli, C. Desgranges, F. Rouillard, K. Ginestar, M. Tabarant, K. Rousseau, Comparative oxidation behaviour of Fe-9Cr steel in CO2 and H2O at 550 C: Detailed analysis of the inner oxide layer, Corros. Sci. 100 (2015) 253–266.
[68] S. Madloch, A. Dorcheh, M. Galetz, Effect of Pressure on Metal Dusting Initiation on Alloy 800H and Alloy 600 in CO-rich Syngas, Oxid. Met. 89 (3–4) (2018) 483–498.
[69] Y. Nishiyama, K. Kitamura, N. Otsuka, Metal dusting behaviour of Alloy800H in laboratory carbonaceous environments under high pressure, Materials Science Forum 595 (2008) 649–660. Trans Tech Publ.
[70] A.R.-V. Put, A. Fabas, S. Doublet, D. Monceau, Relevance of other parameters than carbon activity in defining the severity of a metal dusting environment, Oxid. Met. 87 (5–6) (2017) 655–666.
[71] K. Natesan, Z. Zeng, Development of materials resistant to metal dusting degradation, Argonne National Lab.(ANL), Argonne, IL (United States), 2007.
[72] A. Paul, K. Kaimal, M. Naik, S. Dharwadkar, Lattice and grain boundary diffusion of chromium in superalloy Incoloy-800, J. Nucl. Mater. 217 (1–2) (1994) 75–81.
[73] N. Parimin, E. Hamzah, A. Amrin, Effect of grain size on the isothermal oxidation of superalloys, Advances in Environmental Biology 7 (12) (2013) 3720–3726.
[74] M.G. Fontana, Corrosion engineering, 1986.
[75] K. Ralston, N. Birbilis, Effect of grain size on corrosion: a review, Corrosion 66 (7) (2010), pp. 075005-075005-13.
[76] S. Splinter, R. Rofagha, N. McIntyre, U. Erb, XPS characterization of the corrosion films formed on nanocrystalline Ni–P alloys in sulphuric acid, Surface and Interface Analysis: An International Journal devoted to the development and application of techniques for the analysis of surfaces, interfaces and thin films 24 (3) (1996) 181–186.